



Research on a Multi-source RFI Mitigation Algorithm Using a Reference Antenna Array

Han Wu^{1,2}, Hai-Long Zhang^{1,2,3,4} , Ya-Zhou Zhang¹ , Jie Wang^{1,2,4} , Xin-Chen Ye^{1,4}, Xu Du^{1,2} , and Ting Zhang^{1,2}

¹ Xinjiang Astronomical Observatory, Chinese Academy of Sciences, Urumqi 830011, China; zhanghailong@xao.ac.cn

² University of Chinese Academy of Sciences, Beijing 100049, China

³ Key Laboratory of Radio Astronomy, Chinese Academy of Sciences, Nanjing 210008, China

⁴ National Astronomical Data Center, Beijing 100101, China

Received 2024 August 19; revised 2024 October 9; accepted 2024 October 12; published 2024 November 5

Abstract

We propose a multi-source radio frequency interference (RFI) mitigation method based on a reference antenna array to address the challenge of RFI from multiple directions in radio observation equipment. It introduces a sampling point correction technique using a multi-channel parallel cross-correlation computation method, enhancing the effectiveness of frequency domain adaptive RFI fast mitigation algorithms. The design implements an RFI component detection method based on cross-correlation coefficient thresholds to effectively reduce new interference frequency components introduced by the reference antenna array. Simulated RFI signals and baseband signals of pulsar J0332+5434 observed by the Nanshan 26 m Radio Telescope (NSRT) were used to test the algorithm proposed in this paper. Simulation results demonstrate that the simulated radio telescope signals after RFI mitigation closely match the original pulsar data in profile and phase, confirming the effectiveness of the proposed method.

Key words: methods: data analysis – techniques: interferometric – (stars:) pulsars: individual

1. Introduction

Nowadays, to expand the boundaries of astronomical observations and explore more distant, deeper, and fainter astronomical signals, radio telescopes have been evolving toward larger apertures, higher sensitivity, and wider bandwidths. However, increasing human radio activities are causing significant radio frequency interference (RFI). RFI sources, closer to radio telescopes and emitting stronger signals compared to astronomical signals, severely degrade the quality of astronomical data. Traditional RFI mitigation methods primarily involve blocking affected frequency channels, especially those affected by narrowband signals from human activities. However, as radio telescope observation bandwidths continue to expand (Price et al. 2018), the electromagnetic environment becomes more complex. This could negatively impact the scientific potential of wideband receivers (Zhang et al. 2024b), reducing the telescope's ability to detect distant celestial objects and faint targets.

Previous scholars have explored various approaches in RFI mitigation. Zhang et al. (2013) proposed establishing a radio-quiet zone around the Five-hundred-meter Aperture Spherical radio Telescope (FAST), effectively reducing ground-based RFI impact, although challenges persist from RFI by artificial Earth satellites (Zhang et al. 2013). Kocz et al. (2010) used a Phased Array Feed (PAF) for spatial filtering to mitigate RFI by reducing the telescope's gain in the RFI direction. This method demands high precision in the telescope's surface and a large number of PAF elements (Wang et al. 2024). When the RFI source is near

the telescope's pointing direction, it is difficult to achieve effective RFI mitigation by simply adjusting the antenna's directional gain. Offringa et al. (2010) introduced methods such as SumThreshold and AOFlagger for the Low-Frequency Array (LOFAR) (Offringa et al. 2023; Zhang et al. 2023b). Yang et al. (2020) achieved high accuracy using deep learning to detect RFI in time-frequency domain plots. Scientists seek to use wideband receivers for broad continuous spectrum signals, but channel blocking methods based on RFI identification may reduce observation bandwidth. Therefore, more researchers are exploring active RFI mitigation methods (Morello et al. 2021).

The adaptive RFI mitigation algorithm is based on the assumption of correlation between a reference interference signal and the radio telescope's interference signal. This method requires the reference antenna to avoid or minimize receiving astronomical signals, akin to spatial filtering (Liu et al. 2024). Adaptive filters can dynamically adjust filter tap coefficients (Zhang et al. 2023a), have wide applications for their effective interference suppression and multipath cancellation in astronomy. Researchers, such as Kesteven et al. (2005), have applied adaptive algorithms to suppress RFI in pulsar observations. Szadkowski (2021) tested adaptive filters using Forward Prediction Error (FPE) and Least Mean Squares (LMS) algorithms on narrowband communication signals with the AERA cosmic-ray detector (Szadkowski 2020). Finger et al. (2018) implemented adaptive filtering on FPGA, achieving real-time suppression of multi-carrier RFI on band-limited signals from FAST.

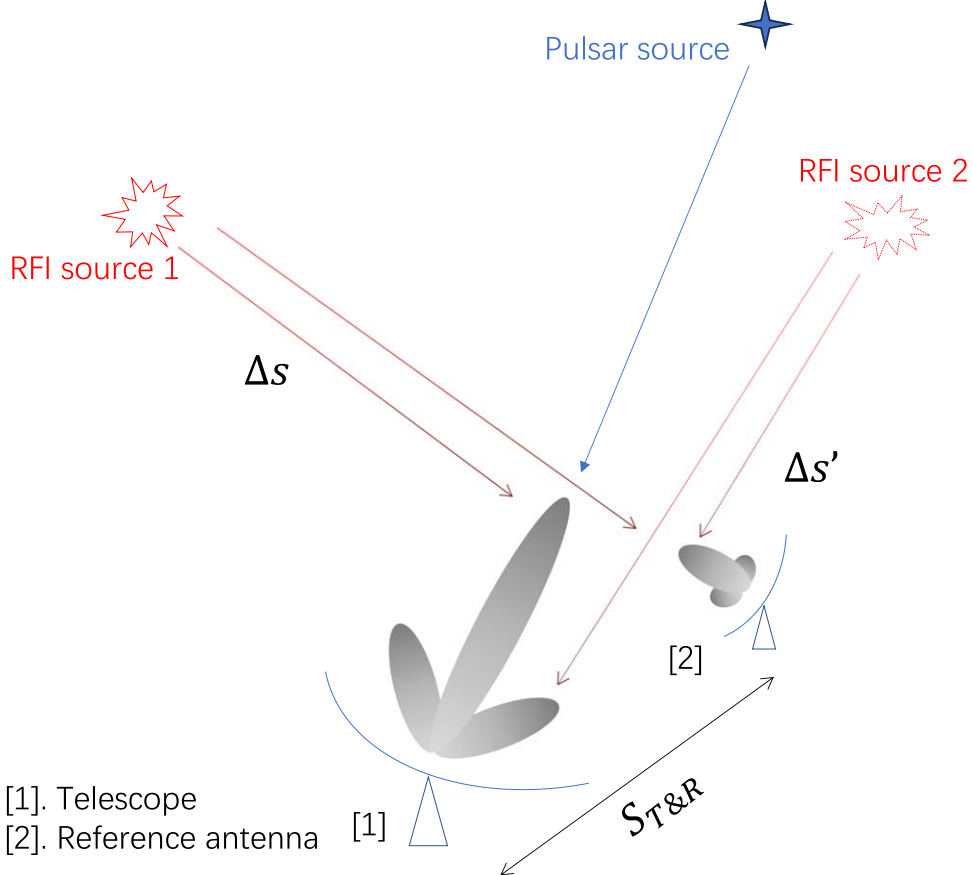


Figure 1. The phase difference of RFI signals between radio telescope and reference antenna is determined solely by the direction of the RFI source.

Wu et al. (2024) found that phase offsets between the reference interference signal and the radio telescope's interference signal greatly affect adaptive RFI mitigation effectiveness. They proposed an RFI algorithm based on phase correction to enhance mitigation efficacy. The phase offset depends on the direction of the RFI source. When the telescope points in a fixed direction, a fixed phase offset can be calculated and corrected using cross-correlation operations for stationary RFI sources. However, real electromagnetic environments at radio telescopes are complex and involve multiple interference sources. For stationary RFI sources in different directions, correcting the phase of a single-reference antenna signal alone cannot align it with all interference components of the radio telescope.

Reference antenna arrays hold promise for addressing the complex interference challenges faced by radio telescopes, including signals from communication base stations with relatively fixed positions on the horizon but variable frequencies, radar signals, and slowly moving mobile communication devices. By further enhancing the aperture and pointing accuracy of the reference antennas, it may also be feasible to utilize reference signal arrays to mitigate satellite RFI.

2. Multi-source RFI Mitigation Algorithm Description

In the case of a single RFI source, the difference in distance to the radio telescope and the reference antenna causes a phase difference in the baseband signals received by both antennas. Equation (1) specifies the sampling point offset resulting from this phase difference

$$P_{\text{offset}} = \left\lceil \frac{\Delta s}{c} \cdot f_s \right\rceil. \quad (1)$$

P_{offset} indicates the sampling point offset of the RFI signal in the baseband signals received by two antennas. Δs represents the distance difference from the RFI source to the two antennas, c is the speed of electromagnetic wave propagation in the medium, f_s denotes the receivers' sampling rate, and $\lceil \rceil$ signifies the ceiling function. In most cases, RFI sources are sufficiently far from the telescope, assuming they are in the far-field region where RFI signals can be treated as plane waves. As shown in Figure 1, when the relative positions between the RFI source and the two antennas remain constant, the only factor affecting the distance difference between the RFI source and the antennas is the direction of the RFI source. When the radio telescope points in a fixed direction, the sampling point

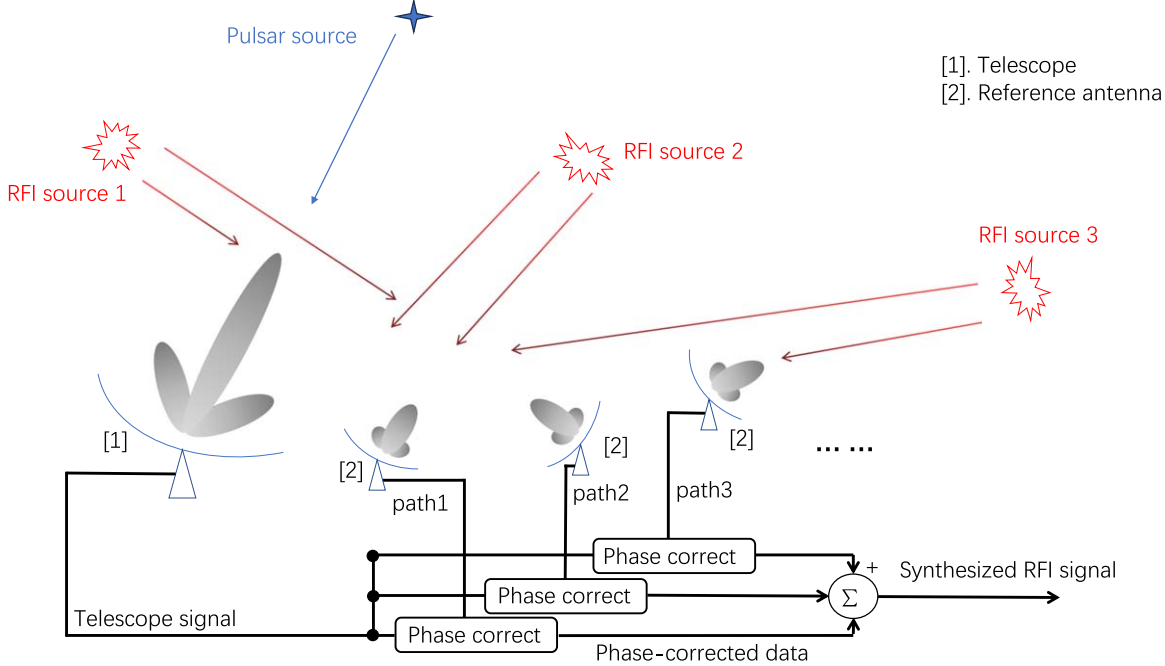


Figure 2. Combining multiple RFI streams into a single RFI signal using a reference antenna array.

offset of the RFI signal in the baseband signals received by the antennas can be computed through cross-correlation operations. When the RFI source, radio telescope, and reference antenna are aligned in a straight line, the sampling point offset of the RFI signal in the baseband signals of the antennas reaches its maximum, as defined by Equation (2)

$$P_{\max_offset} = \left\lceil \frac{S_{T\&R}}{c} \cdot f_s \right\rceil. \quad (2)$$

P_{\max_offset} represents the maximum possible sampling point offset, and $S_{T\&R}$ denotes the distance between the radio telescope and the reference antenna. The number of points for cross-correlation operations should exceed the maximum possible sampling point offset, due to computational constraints, typically set at 15–25 times P_{\max_offset} . In this paper, N is taken as $20 * P_{\max_offset}$, with fewer points required for higher interference signal power.

With multiple RFI sources from different directions simultaneously present, a single aperture reference antenna can only capture one data stream, unable to separate RFI signal components with different sampling point offsets. One approach is to use multiple reference antennas based on the spatial filtering concept. These antennas are positioned in different directions to obtain multiple streams of RFI reference signals. Each stream undergoes separate sampling point offset correction before being combined into a single RFI reference signal, as illustrated in Figure 2.

Let x denote the signal received by the radio telescope in Figure 2, and let r_1 , r_2 , and r_3 denote the signals received by the

reference antennas. The sampling point offset calculation formula is as follows

$$O_j = N - 1 - \left\{ \arg \max_n \left[\sum_{i=0}^{2N-2} x^*(i) r_j(i+n) \right] \right\}, \\ n \in \{0, 1, \dots, 2N-2\} \quad (3)$$

where $\arg \max_n$ represents the value of n when the expression inside the parentheses reaches its maximum, and N denotes the number of points involved in the sampling point offset calculation between the radio telescope signal and the reference antenna signal, $N > P_{\max_offset}$. r_j represents the j th reference antenna signal, $j \in \{1, 2, \dots, k\}$, where k denotes the number of reference antennas. O_j denotes the offset in samples of the j th reference antenna signal relative to the homologous RFI signal in the radio telescope signal. The formula for the synthesized reference RFI signal is given as follows

$$r(n) = \sum_{j=1}^k r_j(n + O_j). \quad (4)$$

In Equation (4), r denotes the combined RFI signal, while the meanings of other symbols remain unchanged.

Using all reference antenna data to synthesize the final reference RFI signal may introduce interference signals that were originally absent in the radio telescope. For instance, when the reference antenna points toward the sidelobe or null direction of the radio telescope, the RFI signal measured by the radio telescope in that direction is typically weaker than that measured by the reference antenna. Including such reference

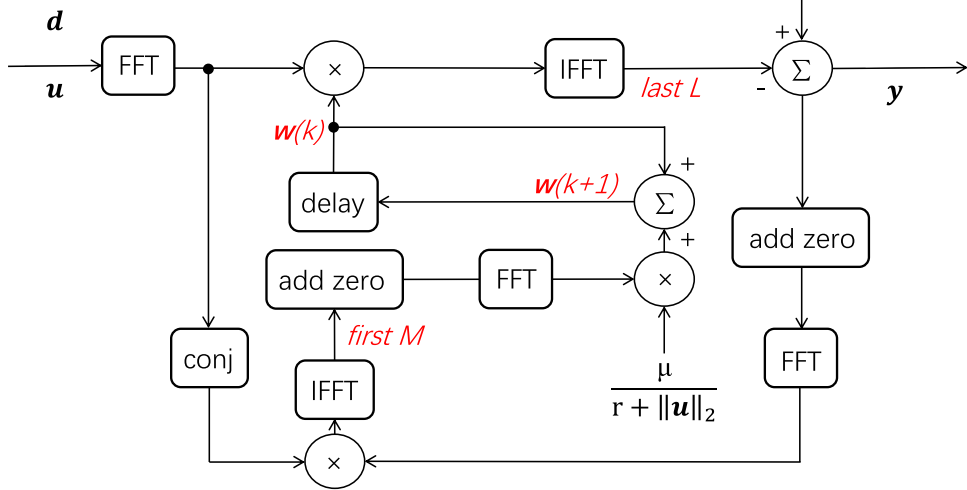


Figure 3. Frequency domain adaptive RFI fast mitigation algorithms.

antenna data in the final baseband reference signal could introduce frequency components not present in the radio telescope. One potential solution is to incorporate correlation detection when calculating phase offsets in Equation (4).

$$r_{xr_j} = \frac{c_{xr_j}}{\sqrt{c_{xx} c_{r_j r_j}}}, j \in \{1, 2, \dots, k\}. \quad (5)$$

In Equation (5), c_{xr_j} denotes the covariance between the radio telescope signal and the RFI component from the j th reference antenna, c_{xx} represents the variance of the radio telescope signal, $c_{r_j r_j}$ is the variance of the j th reference antenna signal, and r_{xr_j} indicates the cross-correlation coefficient between the radio telescope signal and the RFI component from the j th reference antenna. If the cross-correlation coefficient falls below a certain threshold, it indicates that the RFI component is not present in the radio telescope signal. As a result, data from that reference antenna are excluded from subsequent RFI signal synthesis steps.

The obtained reference RFI signals are subjected to frequency domain adaptive RFI fast mitigation as depicted in Figure 3. Here, M denotes the filter order, and L represents the length of data processed each time, both set to 64 for this experiment. $\mathbf{u} \in \mathbb{C}^{L+M}$ denotes the reference RFI signal. $\mathbf{d} \in \mathbb{C}^L$ represents the radio telescope signal. $\mathbf{y} \in \mathbb{C}^L$ signifies the output data after RFI mitigation. The “add zero” operation extends the input data length to $L+M$ by padding zeros, while “delay” introduces a one-cycle delay for the input. $\mathbf{W} \in \mathbb{C}^{L+M}$ signifies the tap coefficients of the adaptive filter. μ stands for the iteration step size of the adaptive filter, set to 0.07 in this experiment, and r is the regularization factor, set to 0.01. $\|\mathbf{u}\|_2$ represents the Euclidean norm of the input signal.

$$\mathbf{W}(k) = [W_0(k) \ W_1(k) \ \dots \ \mathbf{0}]^T, \quad (6)$$

$$\mathbf{U}(k) = \text{FFT}([\mathbf{u}(kL - M) \ \dots \ \mathbf{u}(kL - 1) \ \mathbf{u}(kL) \ \dots \ \mathbf{u}(kL + L - 1)])^T, \quad (7)$$

where $\mathbf{U} \in \mathbb{C}^{L+M}$, $\mathbf{0}$ is the zero vector. In Equation (6), k denotes the current data block index, superscript T indicates matrix transpose, and “FFT” denotes Fast Fourier Transform.

$$\mathbf{y} = \text{IFFT}(\mathbf{U}(k) \odot \mathbf{W}(k)) \text{ last } L \text{ elements}, \quad (8)$$

where \odot denotes element-wise vector multiplication, known as the Hadamard product, and “IFFT” represents the Inverse Fast Fourier Transform. The operation extracts the last L value from the result, hence $\mathbf{y} \in \mathbb{C}^L$.

$$\mathbf{e}(k) = [e(kL) \ e(kL + 1) \ \dots \ e(kL + L - 1)]^T = \mathbf{d} - \mathbf{y}, \quad (9)$$

$$\mathbf{E}(k) = \text{FFT}([\mathbf{0} \ e(kL) \ \dots \ e(kL + L - 1)]^T), \quad (10)$$

$$\Phi(k) = \text{IFFT}(\text{conj}(\mathbf{U}(k)) \odot \mathbf{E}(k)) \text{ first } M \text{ elements}, \quad (11)$$

$$\mathbf{W}(k + 1) = \mathbf{W}(k) + \frac{\mu}{r + \|\mathbf{u}\|_2} \cdot \text{FFT} \left[\begin{matrix} \Phi(k) \\ \mathbf{0} \end{matrix} \right], \quad (12)$$

where $\mathbf{e} \in \mathbb{C}^L$ denotes the error matrix between the radio telescope signal and the filter input signal. $\mathbf{E} \in \mathbb{C}^{L+M}$, and in Equation (10), $\mathbf{0} \in \mathbb{C}^{L+M}$. $\|\cdot\|_2$ represents the Euclidean norm, and “conj” denotes conjugation. Let Φ denote the cross-correlation matrix between the filter input signal and the error signal. We take the first M values of the operation result, hence $\Phi \in \mathbb{C}^M$. In Equation (12), the zero vector $\mathbf{0} \in \mathbb{C}^L$. Adding regularization and normalization factors during the filter coefficient iteration process can effectively enhance the algorithm’s robustness.

3. Nanshan 26 m Radio Telescope Baseband Data Testing

Part of the baseband observation data of pulsar J0332+5434 from Nanshan 26 m Radio Telescope (NSRT; Zhang et al. 2024a) was captured as an astronomical signal in the simulation experiment. Because the interference signals are generated by

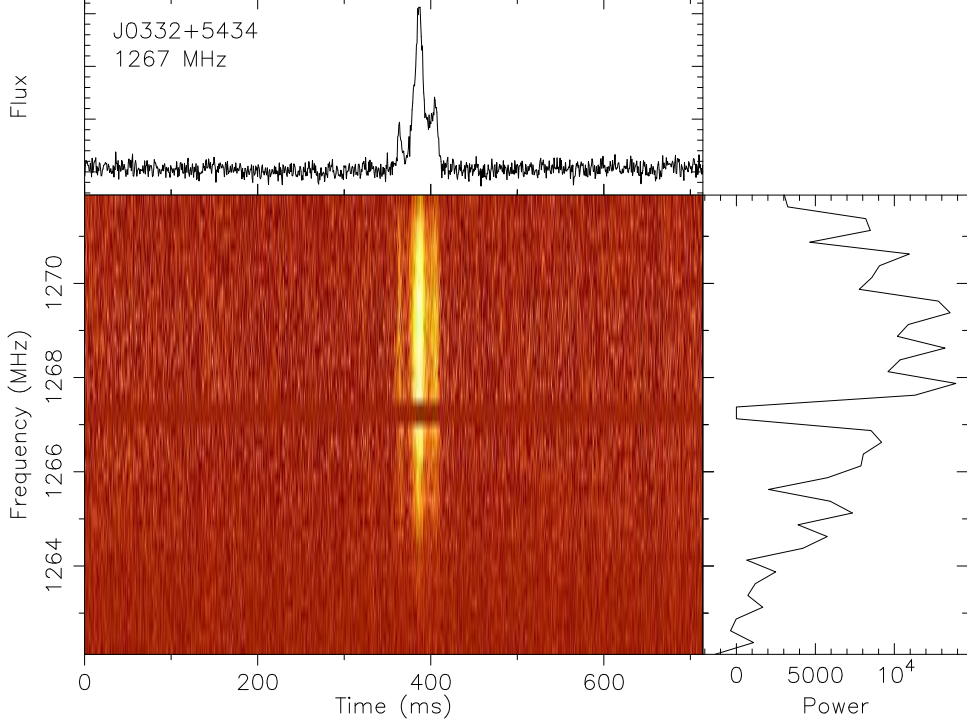


Figure 4. Dynamic spectrum of raw pulsar data.

Table 1
Basic Information on Pulsar Data

Parameter	Value
Source	J0332+5434
Center Freq	1267 MHz
Bandwidths	10 MHz
NBIT	16
NPOL	1
DM	$26.7641 \text{ cm}^{-3} \text{ pc}$
Length	4 minutes

simulation, a segment of the single-polarization data from the ultra-wideband receiver with a 10 MHz bandwidth and minimal interference was chosen. Specific parameters are listed in Table 1, and the dynamic spectrum is shown in Figure 4.

3.1. Simulated RFI Signals

Due to hardware constraints, the experiment simulated seven RFI signals. Each signal was generated using complex frequency-sweep simulations, with parameters detailed in Table 2.

Add RFI1 to RFI5 from Table 2 to the astronomical data, simulate five random RFIs received by the radio telescope, and add RFI8 from Table 2 to the data to simulate the broadband RFI received by the telescope. The simulated spectrum of the radio

Table 2
Parameters for Eight Simulated RFI Signals

RFI Type	Start Frequency/MHz	Cutoff Frequency/MHz	Amplitude
RFI1	1269.5	1269.6	4000
RFI2	1263.0	1263.5	5200
RFI3	1263.4	1263.6	4000
RFI4	1263.7	1263.9	5200
RFI5	1263.7	1264.2	3600
RFI6	1265.5	1266.2	8000
RFI7	1266.1	1266.3	4800
RFI8	1263.0	1271.0	5200

telescope signal is depicted in Figure 5, while the spectrum of simulated RFI signals in the radio telescope is shown on the left side of Figure 6. Attenuate the real and imaginary parts of RFI1 to RFI7 from Table 2 to simulate seven random RFIs measured by small-aperture reference antennas, shown on the right side of Figure 6. RFIs from different directions exhibit sampling point offsets in both the radio telescope and reference antennas, so random sampling point offsets are added when generating reference antenna RFI signals. The entire simulated RFI generation process is illustrated in Figure 7.

3.2. Synthesized Based RFI Reference Signal

Calculate the cross-correlation coefficients between the seven reference antenna signals (ref_RFI) generated in

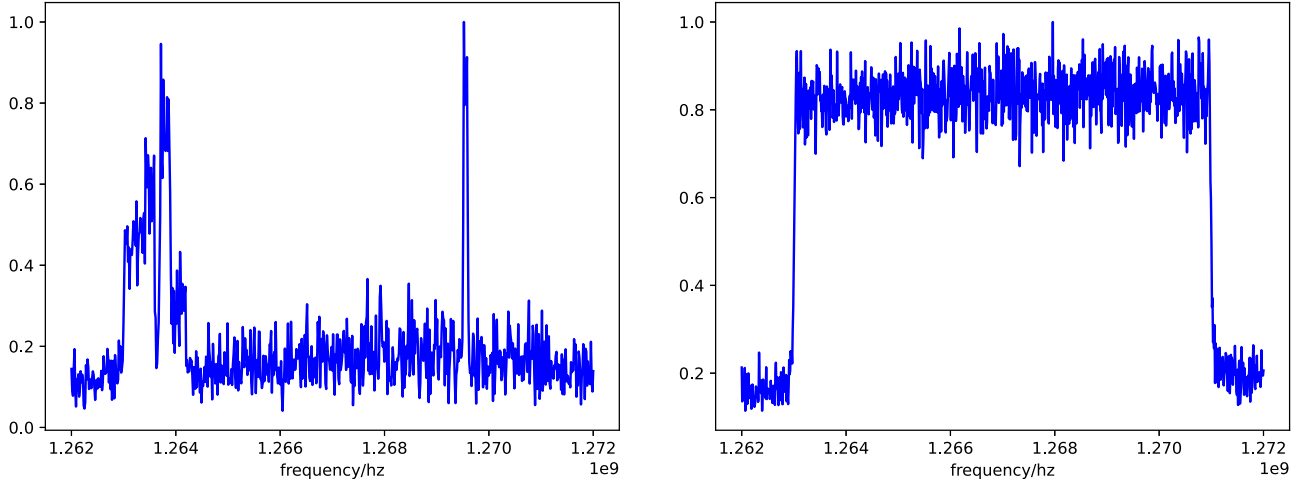


Figure 5. Normalized spectrum of the NSRT baseband signal with simulated RFI signals (left) and broadband RFI signals (right).

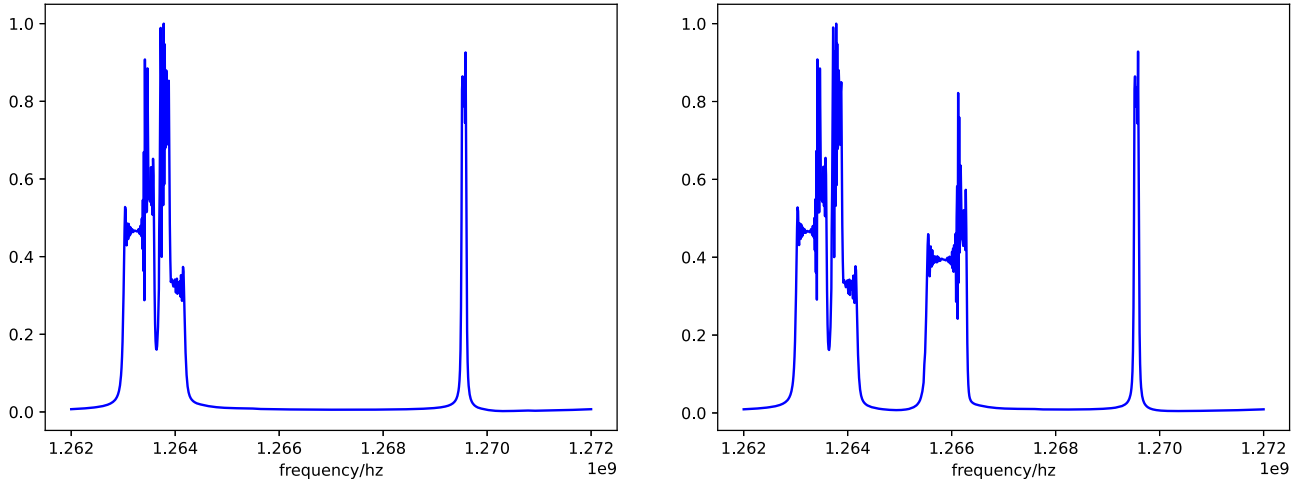


Figure 6. Normalized spectrum of simulated RFI signals in the radio telescope (left) and in the reference antenna array (right).

Section 3.1 and the radio telescope signal, then compute their absolute values to obtain the data presented in Table 3.

In Section 3.1, it is evident that the radio telescope signal does not include RFI6 and RFI7 components. Introducing *ref_RFI6* and *ref_RFI7* during the RFI signal synthesis process introduces new interference into the radio telescope signal, significantly compromising the quality of astronomical data. From Table 3, it is evident that the cross-correlation coefficients between *ref_RFI6*, *ref_RFI7*, and the radio telescope signal are notably lower compared to other reference antenna signals. This indicates that cross-correlation coefficients can be used to determine whether an interference component from a specific reference antenna exists in the radio telescope signal. For this simulation experiment, a cross-correlation coefficient threshold of 0.01 is chosen. Reference signals with cross-correlation coefficients below 0.01 are discarded and not included in the final synthesized baseband

Table 3
Correlation Coefficients Between Simulated Reference Antenna Signals and Simulated Radio Telescope Signals

Reference RFI Type	Coefficient
<i>ref_RFI1</i>	0.223
<i>ref_RFI2</i>	0.069
<i>ref_RFI3</i>	0.276
<i>ref_RFI4</i>	0.362
<i>ref_RFI5</i>	0.091
<i>ref_RFI6</i>	0.002
<i>ref_RFI7</i>	0.004

RFI reference signal. Apply the sampling point offset operation to the remaining *ref_RFI* signals as described in Equation (3). Use the results in Equation (4) to synthesize the RFI reference signal, combining multiple reference antenna signals into a

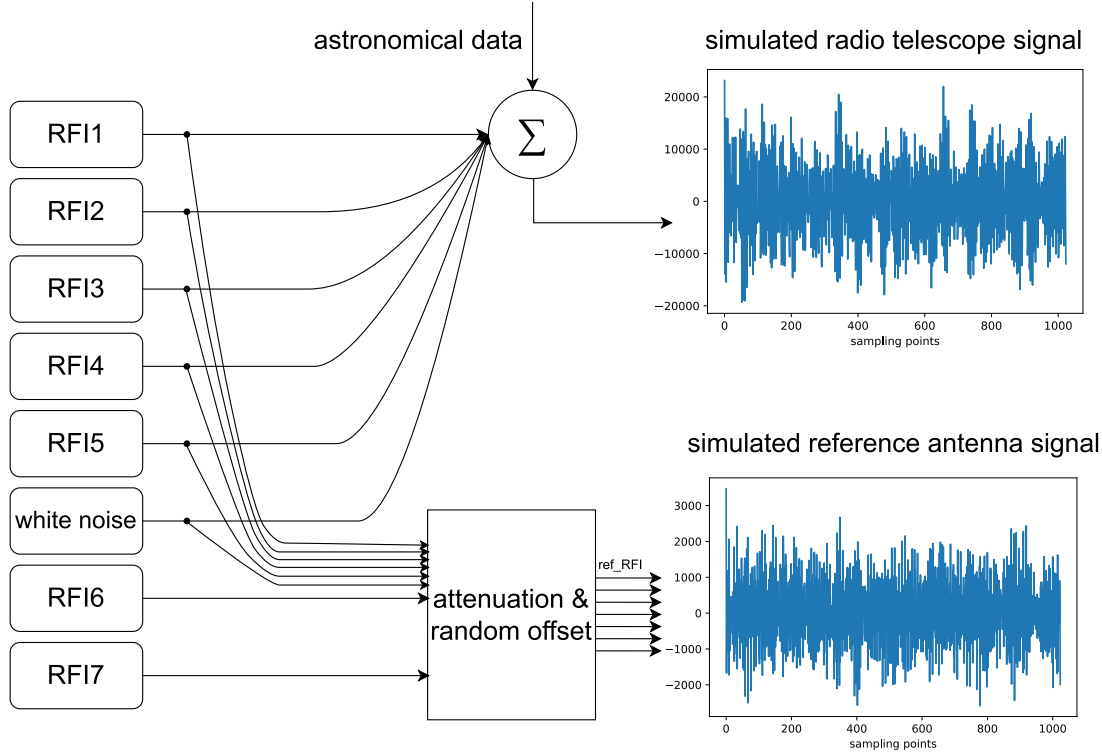


Figure 7. Simulated RFI signal generation process, time-domain RFI signals in the radio telescope and reference antenna.

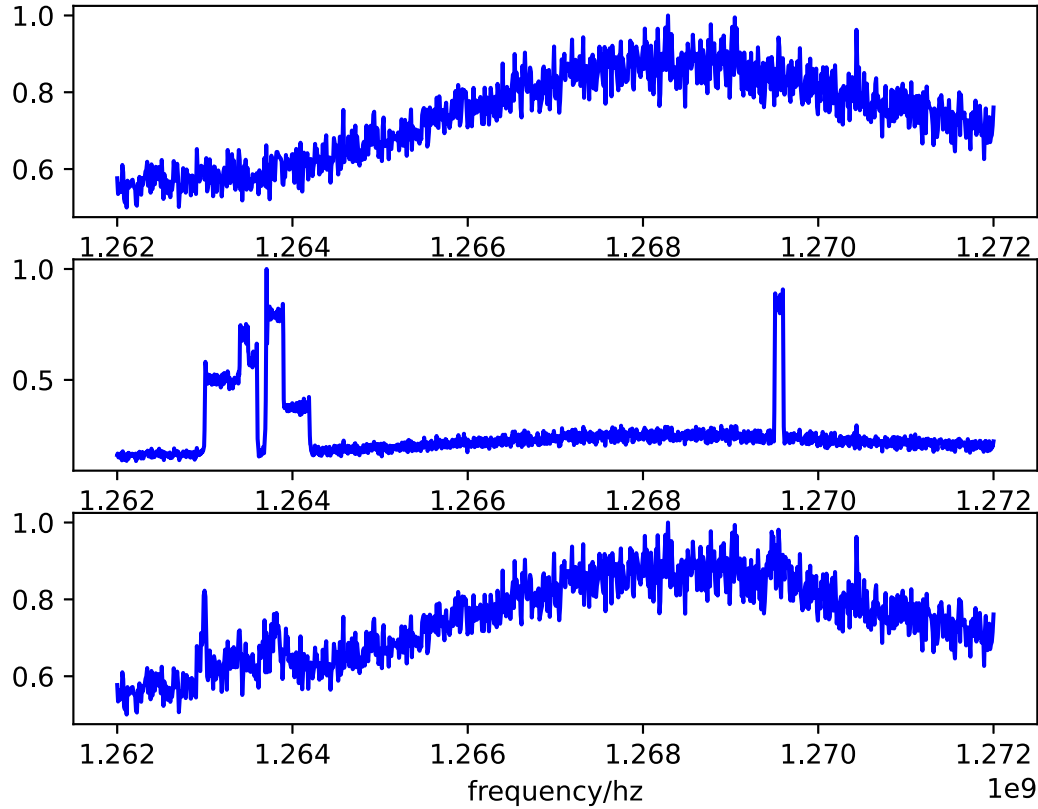


Figure 8. The normalized spectrum of raw pulsar baseband data (top), simulated radio telescope data spectrum after adding RFI signals (middle), and pulsar spectrum after RFI mitigation using sampling point offset correction and RFI component detection algorithms (bottom).

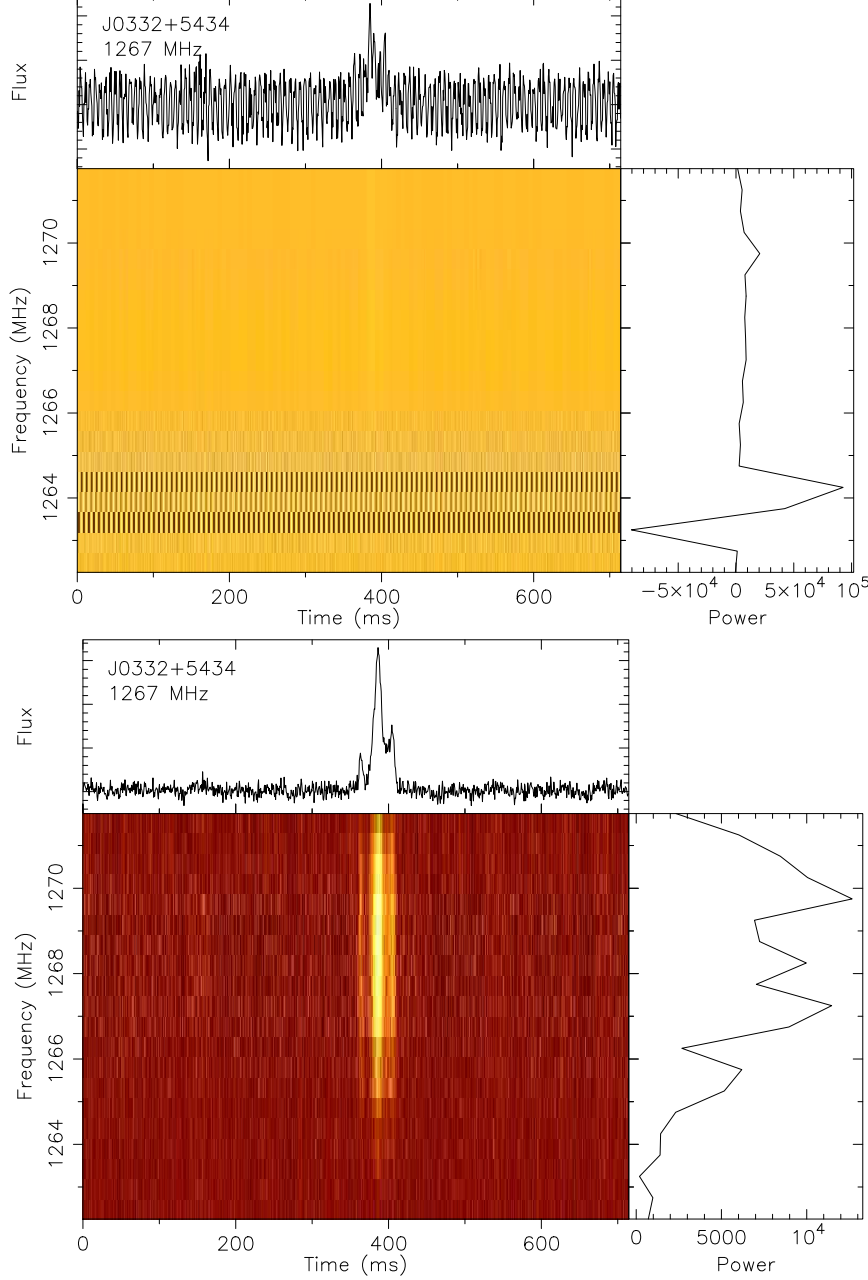


Figure 9. Dynamic spectrum of simulated radio telescope signal with added RFI signals (top), and after RFI mitigation (bottom).

single baseband RFI reference signal with phase alignment. Calculating the correlation coefficients and sampling point offsets involves a significant computational load, making real-time computation impractical and unnecessary. Under conditions where the radio telescope remains stationary and RFI sources are relatively static or move slowly, these coefficients and offsets remain stable. In practical applications, the computation interval can be adjusted based on these conditions.

4. Results Analysis

The adaptive RFI mitigation algorithm, implemented on an NVIDIA 3090 GPU, leverages its high parallel processing capability for efficient handling of large-scale astronomical data. Figure 8 shows the spectrum of raw pulsar baseband data, the simulated radio telescope data spectrum after adding RFI signals, and the spectrum of the pulsar data after RFI

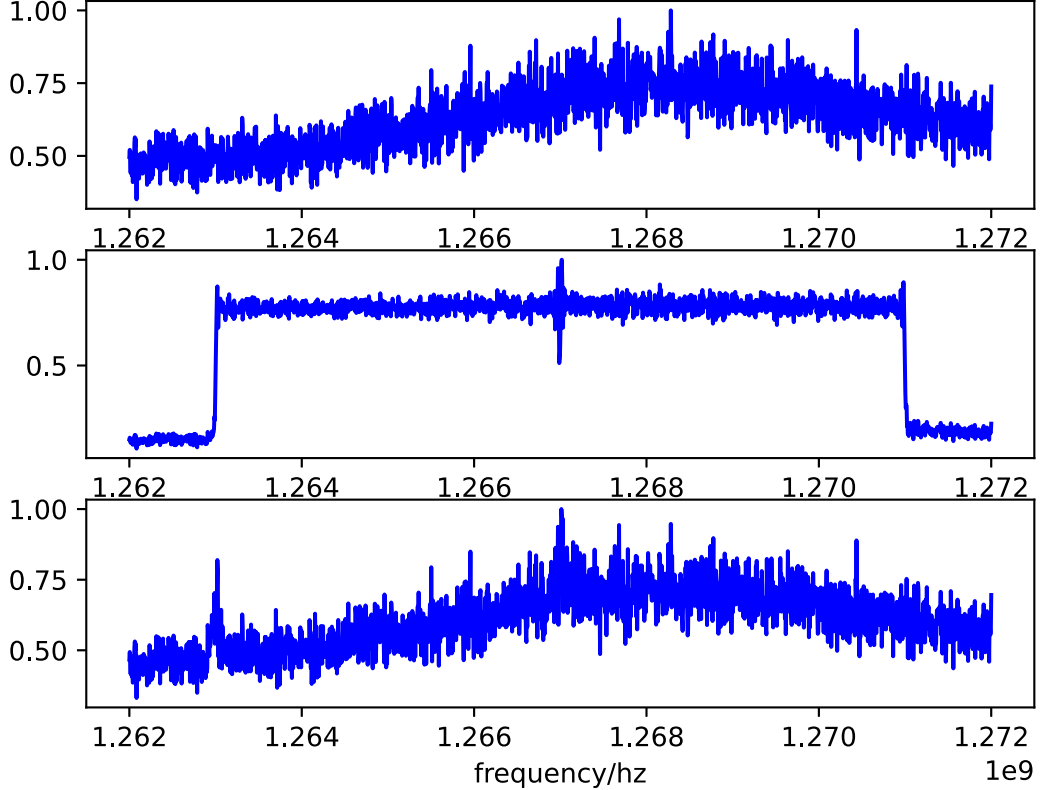


Figure 10. The normalized spectrum of raw pulsar baseband data (top), simulated radio telescope data spectrum after adding broadband RFI signals (middle), and pulsar spectrum after RFI mitigation using sampling point offset correction and RFI component detection algorithms (bottom).

mitigation. The spectrum shows that the RFI mitigation algorithm effectively removed the simulated RFI signals from the raw pulsar baseband data without introducing new interference or affecting other pulsar frequency components. In Figure 8, after RFI mitigation, only slight deviations are seen at the interference frequencies, while other frequency components closely match the original pulsar baseband data.

In Figure 9, it is clear that the added simulated RFI signals heavily impacted the pulsar profile. After RFI mitigation using the RFI component detection and sampling point offset correction algorithm (Figure 9, bottom), the pulsar profile closely matches the one in Figure 4. Figure 10 illustrates the effectiveness of the RFI mitigation algorithm on broadband interference signals. The spectrum and dynamic spectrum in Figures 10 and 11 indicate that the proposed RFI mitigation algorithm is also effective against broadband interference signals.

4.1. The Impact of Sampling Point Alignment on the Effectiveness of RFI Mitigation

To illustrate the critical role of sampling point offset correction in RFI mitigation for radio telescopes, Figure 12 shows the spectrum after RFI mitigation without using sampling point offset correction, along with the original pulsar

spectrum and the spectrum of the simulated radio telescope signal after adding RFI signals.

Wu et al. (2024) treat RFI suppression as a system identification problem. When there is a sampling point offset between the reference antenna and the RFI signals in the radio telescope, this problem transforms into a prediction problem, potentially reducing RFI mitigation effectiveness. Figure 13 illustrates the dynamic spectrum of pulsars obtained using this approach.

4.2. The Effect of Interference Introduced by the Reference Antenna Array on RFI Mitigation Effectiveness

To demonstrate the crucial role of RFI component detection algorithms in radio telescope RFI mitigation, Figure 14 shows the spectrum of the simulated radio telescope signal after adding RFI signals, simulated reference RFI signals, and after RFI mitigation.

Observing Figure 14, it can be noted that the simulated reference RFI signals contain frequency components from 1265.5 to 1266.3 MHz that are not present in the simulated radio telescope signal. These components impact the spectrum of the pulsar signal after interference mitigation. Furthermore, these new interference components alter the original reference

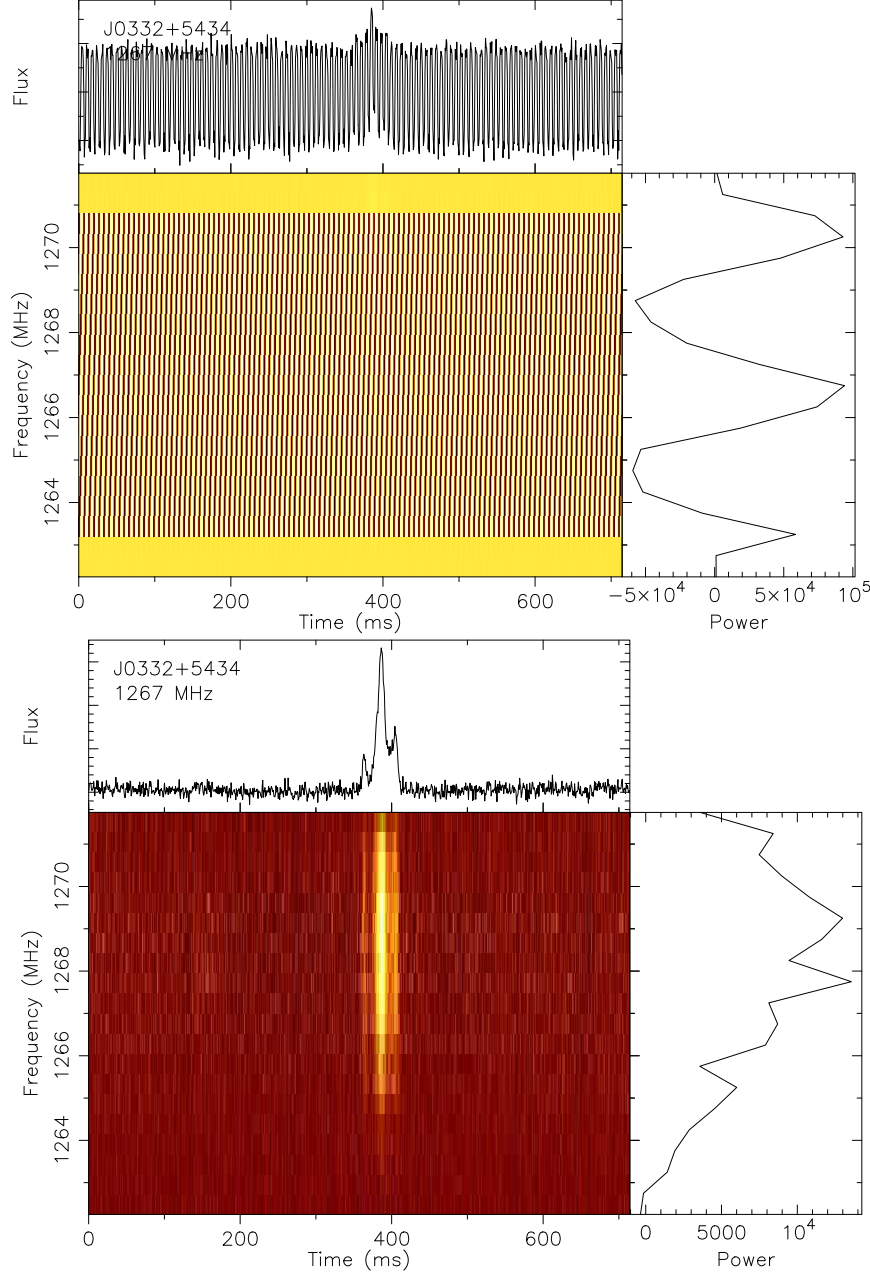


Figure 11. Dynamic spectrum of simulated radio telescope signal with added broadband RFI signals (top), and after RFI mitigation (bottom).

signal power, thereby reducing the mitigation algorithm's effectiveness on other interference frequencies. Using the reference signals depicted in the middle of Figure 14 for RFI mitigation produces the dynamic spectrum of the pulsar shown in Figure 15.

In Figure 16, compared to the simulated radio telescope signal spectrum with RFI component detection algorithms applied for mitigation, the spectrum obtained without these algorithms shows new frequency components near 1266 MHz that are not originally present in the simulated radio telescope signal. These

components are introduced by the reference interference signals depicted in the middle panel of Figure 14. However, due to their relatively low amplitude, their impact on the pulsar profile after folding integration is minimal.

The SNR values in Table 4 are calculated using PSRCHIVE.⁵ Table 4 shows that sampling point offset correction significantly improves RFI mitigation, while the RFI component detection algorithm has only a limited impact on pulsar profile quality.

⁵ <https://psrchive.sourceforge.net/>

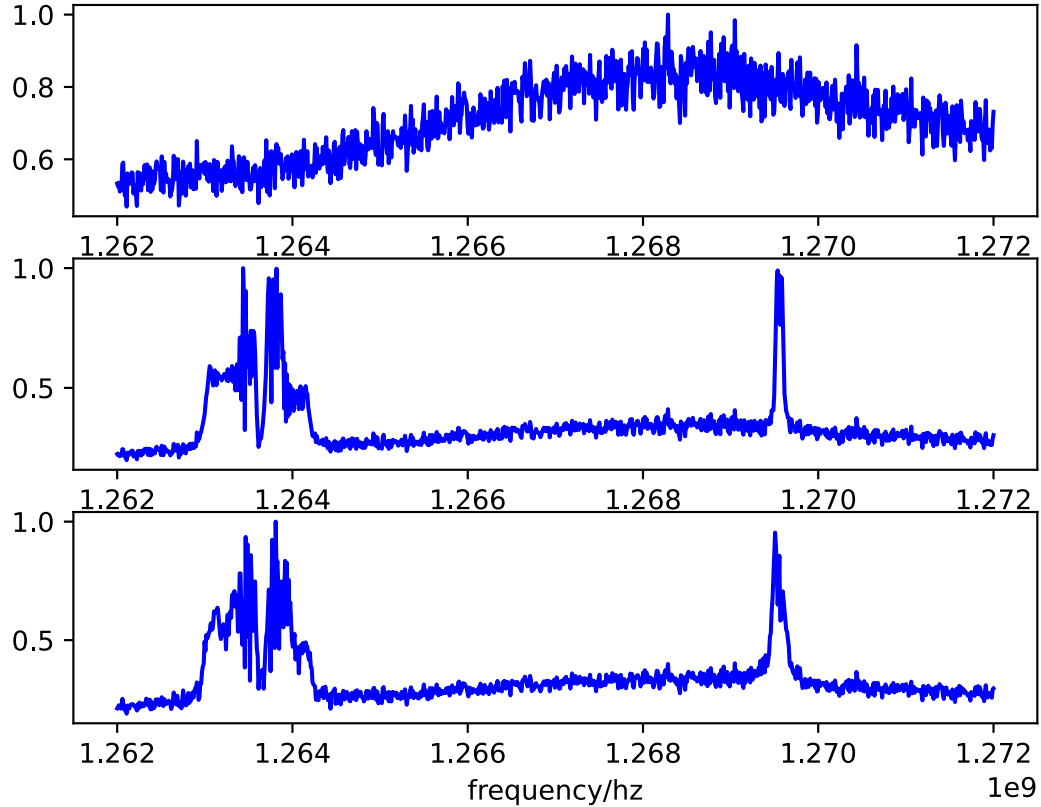


Figure 12. The normalized spectrum of raw pulsar baseband data (top), simulated radio telescope data spectrum after adding RFI signals (middle), and pulsar spectrum after RFI suppression using only the RFI component detection algorithm, without sampling point offset correction (bottom).

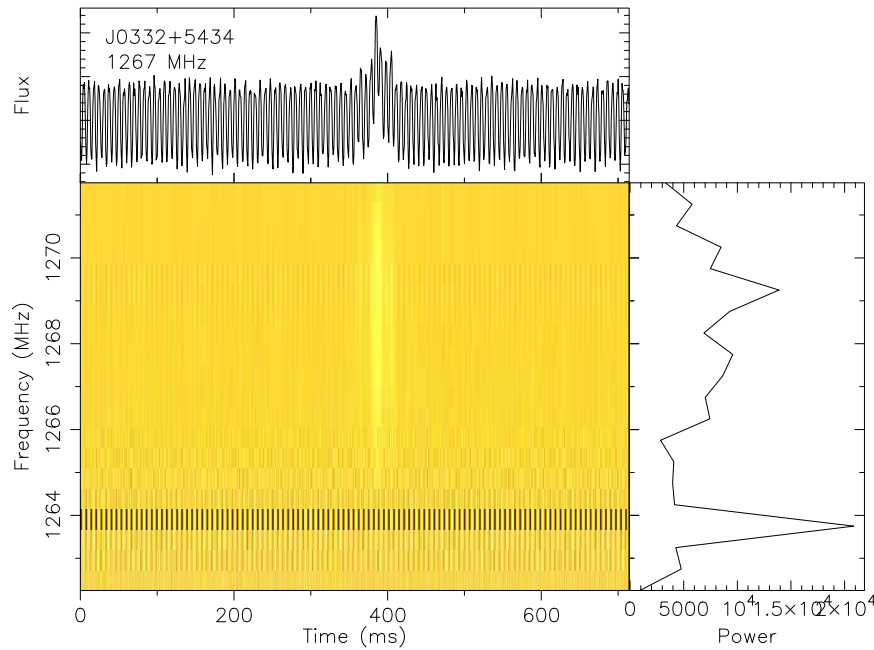


Figure 13. Dynamic spectrum of simulated radio telescope signal after RFI mitigation without sampling point offset correction.

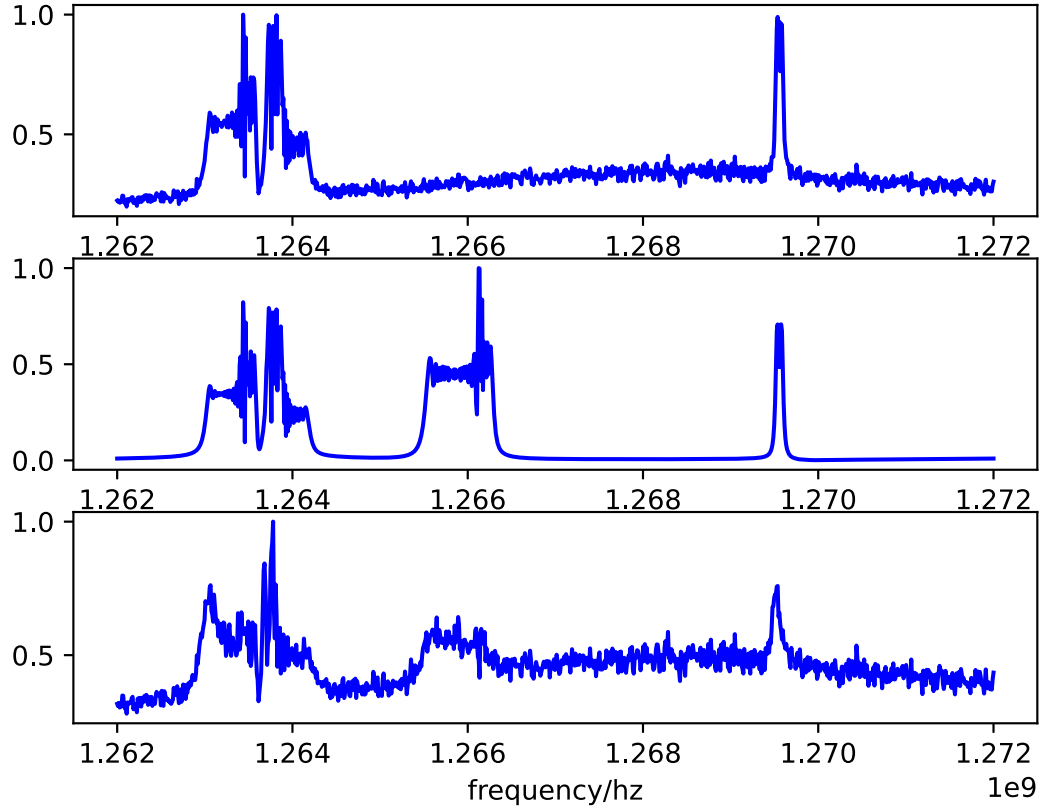


Figure 14. The normalized spectrum of the simulated radio telescope signal after adding RFI signals (top), simulated reference RFI signals (middle), and after RFI mitigation (bottom).

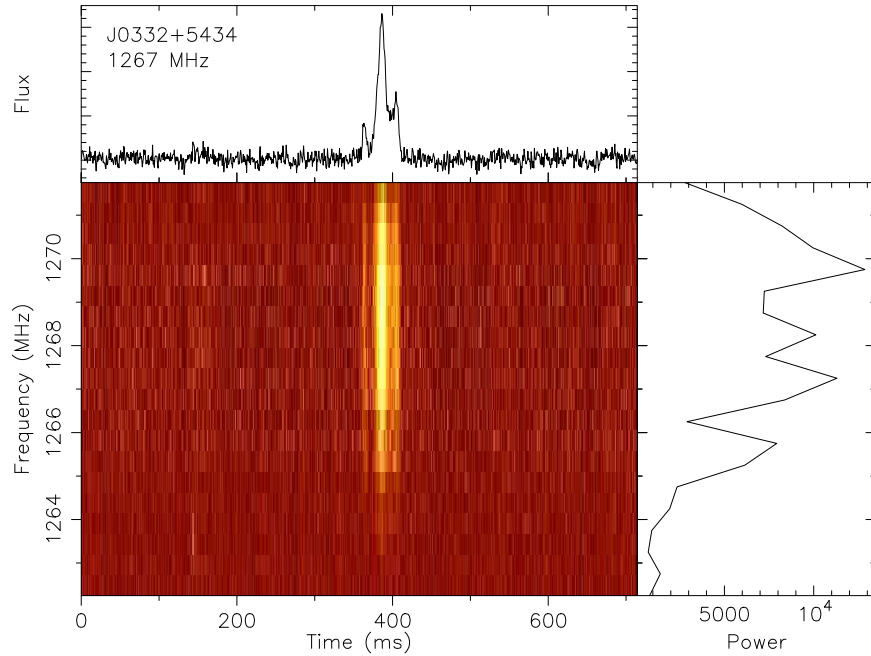


Figure 15. The dynamic spectrum generated from the simulated radio telescope signal after applying the sampling point offset correction algorithm and without using RFI component detection algorithms for RFI mitigation.

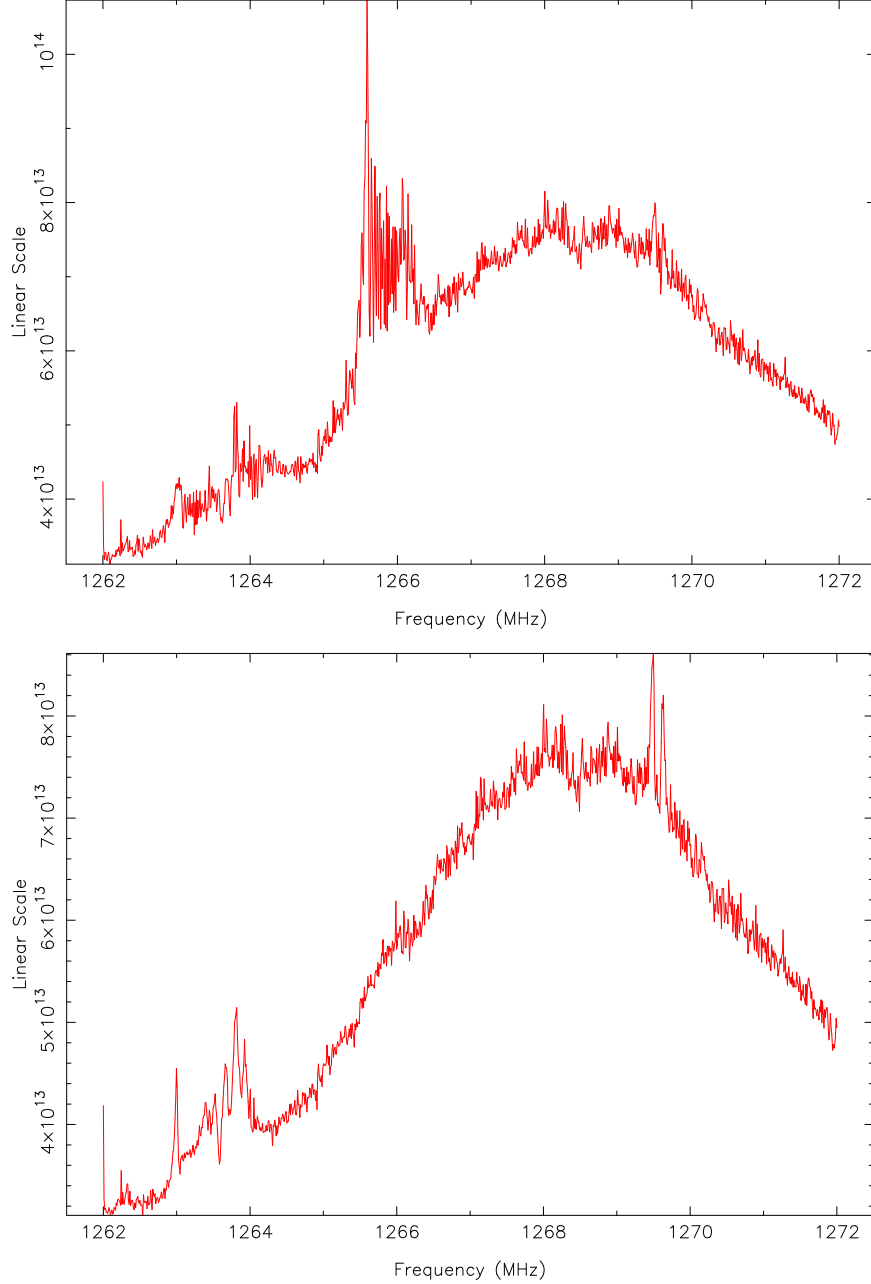


Figure 16. Spectrum of the simulated radio telescope signal after RFI mitigation using only sampling point offset correction (top), and spectrum of the simulated radio telescope signal after RFI mitigation using both sampling point offset correction and RFI component detection (bottom).

Table 4
The Signal-to-Noise Ratio (SNR) Calculated by PSRCHIVE

Signal Type	SNR
Original signal	46.3
Original signal with added RFI signals	3.6
Original signal with added broadband RFI signals	2.2
Using only sampling point offset correction	41.7
Using only the RFI detection algorithm	3.7
Using both methods	43.3
Using both methods in the broadband RFI scenario	46.0

However, as demonstrated in Figure 16, RFI component detection significantly enhances the quality of the spectrum.

5. Conclusions

This paper introduces a multi-source RFI suppression method based on a reference antenna array, focusing on addressing complex RFI challenges in radio telescope observations. Experimental verification was conducted using baseband data of pulsar J0332+5434 observed by NSRT and simulated

complex swept-frequency RFI signals. The study reveals that traditional single-reference antennas struggle to capture interference signals from all directions and cannot correct sampling point offsets for specific directional RFI signals. In contrast, using a reference antenna array allows for separate correction of RFI signals from different directions and sampling point offsets, synthesizing a baseband reference signal where all RFI components are aligned. This significantly enhances the effectiveness of the frequency-domain adaptive RFI fast mitigation algorithm. Additionally, to address the issue of potential new interference introduced by the reference antenna array, this paper proposes an RFI component detection algorithm. By setting a cross-correlation coefficient threshold, it determines whether RFI components detected by various reference antennas are present in the radio telescope signal, effectively preventing the introduction of new interference signals. This ensures the robustness and reliability of the mitigation algorithm.

Acknowledgments

This work is supported by the National Key R&D Program of China Nos. 2021YFC2203502 and 2022YFF0711502; the National Natural Science Foundation of China (NSFC, grant Nos. 12173077, 12073067); the Tianshan Talent Project of Xinjiang Uygur Autonomous Region (2022TSYCCX0095 and 2023TSYCCX0112); the Scientific Instrument Developing Project of the Chinese Academy of Sciences, grant No. PTYQ2022YZZD01; China National Astronomical Data Center (NADC); the Operation, Maintenance and Upgrading

Fund for Astronomical Telescopes and Facility Instruments, budgeted from the Ministry of Finance of China (MOF) and administrated by the Chinese Academy of Sciences (CAS); Natural Science Foundation of Xinjiang Uygur Autonomous Region (2022D01A360).

ORCID iDs

- Hai-Long Zhang  <https://orcid.org/0000-0002-8951-7094>
 Ya-Zhou Zhang  <https://orcid.org/0000-0001-6046-2950>
 Jie Wang  <https://orcid.org/0000-0003-0380-6395>
 Xu Du  <https://orcid.org/0000-0001-6448-0822>

References

- Finger, R., Curotto, F., Fuentes, R., et al. 2018, *PASP*, **130**, 1
 Kesteven, M., Hobbs, G., Clement, R., et al. 2005, *RaSc*, **40**, RS5S06.1
 Kocz, J., Briggs, F. H., & Reynolds, J. 2010, *AJ*, **140**, 2086
 Liu, J., Chen, W., Zhang, Y., et al. 2024, arXiv:2406.03144
 Morello, V., Rajwade, K. M., & Stappers, B. W. 2021, *MNRAS*, **510**, 1393
 Offringa, A., Adebarh, B., Kutkin, A., et al. 2023, *A&A*, **670**, A166
 Offringa, A. R., de Bruyn, A. G., Biehl, M., et al. 2010, *MNRAS*, **405**, 155
 Price, D. C., MacMahon, D. H., Lebofsky, M., et al. 2018, *PASA*, **35**, e041
 Szadkowski, Z. 2020, *ITNS*, **67**, 405
 Szadkowski, Z. 2021, *NIMPA*, **999**, 165171
 Wang, K., Cao, L., Ma, J., et al. 2024, *RAA*, **24**, 045005
 Wu, H., Zhang, H.-L., Zhang, Y.-Z., et al. 2024, *RAA*, **24**, 015021
 Yang, Z., Yu, C., Xiao, J., & Zhang, B. 2020, *MNRAS*, **492**, 1421
 Zhang, C., He, J., Liang, Y., Wang, Z., & Xie, X. 2023a, *ApSci*, **13**, 23
 Zhang, H., Nan, R., Peng, B., et al. 2013, in Asia-Pacific Symp. on Electromagnetic Compatibility (APEMC), 1 (Piscataway, NJ: IEEE)
 Zhang, P., Offringa, A. R., Zucca, P., Kozarev, K., & Mancini, M. 2023b, *MNRAS*, **521**, 630
 Zhang, Y.-Z., Zhang, H.-L., Wang, J., et al. 2024a, *RAA*, **24**, 015025
 Zhang, Y.-Z., Zhang, H.-L., Wang, J., et al. 2024b, *RAA*, **24**, 075011